Title: **Mechanical matching of implant to host minimises foreign body reaction**

One sentence summary: Foreign body reaction to medical implants can be avoided by matching the stiffness of the implant surface to that of the host tissue.

Authors: Alejandro Carnicer-Lombarte[1,2,†], Damiano G. Barone[1,3,†], Ivan B. Dimov[2], Russell S. Hamilton[4], Malwina Prater[4], Xiaohui Zhao[4], Alexandra L. Rutz[5], George G. Malliaras[5], Stephanie P. Lacour[6], Clare E. Bryant[3], James W. Fawcett[1,7,*], Kristian Franze[2,*].

[1]John van Geest Centre for Brain Repair, Department of Clinical Neurosciences, University of Cambridge, Cambridge CB2 0PY, UK.

[2]Department of Physiology Development and Neuroscience, University of Cambridge, Cambridge CB2 3DY, UK.

[3]Department of Veterinary Medicine, University of Cambridge, Madingley Road, Cambridge CB3 0ES, UK.

[4]Centre for Trophoblast Research, University of Cambridge, Cambridge, CB2 3EG, UK.

[5]Electrical Engineering Division, Department of Engineering, University of Cambridge, Cambridge CB3 0FA, UK.

[6]Bertarelli Foundation Chair in Neuroprosthetic Technology, Laboratory for Soft Bioelectronics Interface, Institute of Microengineering, Institute of Bioengineering, Centre for Neuroprosthetics, Ecole Polytechnique Fédérale de Lausanne (EPFL), 1202 Geneva, Switzerland.

[7] Centre for Reconstructive Neuroscience, Institute for Experimental Medicine CAS, Prague, Czech Republic

[†] These authors contributed equally to this work.

* To whom correspondence should be addressed: jf108@cam.ac.uk, kf284@cam.ac.uk

Abstract

Medical implants offer a unique and powerful therapeutic approach in many areas of medicine. However, their lifetime is often limited as they may cause a foreign body reaction (FBR) leading to their encapsulation by scar tissue[1–4]. Despite the importance of this process, how cells recognise implanted materials is still poorly understood[5,6]. Here, we show how the mechanical mismatch between implants and host tissue leads to FBR. Fibroblasts and macrophages, which are both crucially involved in mediating FBR, became activated when cultured on materials just above the stiffness found in healthy tissue. Coating implants with a thin layer of hydrogel or silicone with a tissue-like elastic modulus of ~1 kPa or below led to significantly reduced levels of inflammation and fibrosis after chronic implantation both in peripheral nerves and subcutaneously. This effect was linked to the nuclear localisation of the mechanosensitive transcriptional regulator YAP *in vivo*. Hence, we identify the mechanical mismatch between implant and tissue as a driver of FBR. Soft implant coatings matching the mechanical properties of host tissue minimized FBR and may be used as a novel therapeutic strategy to improve long-term biomedical implant stability without extensive modification of current implant manufacturing techniques, thus facilitating clinical translation.

Introduction

Medical implants have become an indispensable tool for a wide range of applications, including bladder control[11], treatment of neurological disorders[12], drug delivery[13], and tissue repair[14]. Recent advances in fabrication techniques have allowed for the development of increasingly complex implants, capable of better integrating into the host tissue and much improved functionality. This is particularly visible in the field of neural interfaces, where implants are capable of establishing electrical connections with individual axons and neurons without disrupting their connectivity[15–17]. Functionality of such implants actively interacting with their environment requires the establishment and maintenance of intimate interfaces between implant and tissue.

However, this interface and thus long-term functionality of medical implants is often limited by foreign body reaction (FBR) – a process by which the body recognises implanted materials as foreign and attempts to degrade them. FBR is characterised by chronic inflammation and fibrosis, and with time results in the formation of a scar – a fibrotic capsule – separating the implant from the host tissue[5]. The breakdown of the tissue-implant interface is one of the leading causes of implant failure[1–3], which has led to efforts to develop a treatment to prevent and manage FBR to implanted materials[18–22]. Impregnation of implants with anti-inflammatory drugs such as dexamethasone is currently used in clinical practice to alleviate inflammatory reactions[23], and suppresses FBR in nerve interfaces[24]. However, such strategies can have significant side effects[24]. Furthermore, how the body recognises implanted materials as foreign and what triggers the associated inflammatory response is still poorly understood[5,6].

Medical implants are usually prepared from materials compatible with miniaturisation, surgical handling and advanced 3D design. These materials are much stiffer than their biological host tissues. Shear moduli, a measure of a material's elastic stiffness, of such implants are usually on the order of hundreds of kPa and above, while most biological

tissues have shear moduli of few kPa[25,26]. While recent studies suggested that softer materials might alleviate inflammation[7–10], a direct link between cellular mechanotransduction and FBR has not been shown yet. Furthermore, how soft materials actually need to be to circumvent FBR is currently not clear, and techniques to manufacture implants using very soft materials are not readily available.

Results

We here investigated whether cell types crucial for FBR in many tissue types, namely primary macrophages and fibroblasts, indeed respond to differences in the stiffness of their environment within a physiologically relevant scale. Macrophages are a central component of innate immunity and are responsible for driving the inflammatory response to implanted materials[5,6]. Fibroblasts, on the other hand, are the primary mediators of the fibrotic response, responsible for the formation of the fibrotic capsule around the implant.

Most macrophages involved in FBR are derived from blood-circulating monocytes, while fibroblasts proliferate from tissue-resident populations[5,6]. We cultured primary bone marrow-derived macrophages and fibroblast populations derived from peripheral nerve tissue on polyacrylamide substrates of a range of shear moduli. Polyacrylamide substrates are well-established essays frequently used to assess cellular responses to the mechanical properties of their environment. We chose nerve fibroblasts because of the high impact of FBR on peripheral nerve interfaces. While implants with shear moduli of few hundreds of kPa are commonly considered ‘soft’[27–29], shear moduli of our substrates ranged from 0.1 kPa, mechanically resembling the softest tissues in the body including peripheral nerve tissue (Supplementary Fig. 1), to 50 kPa, which is already stiffer than most soft tissues and organs[26] (substrate stiffness measurements are shown in Supplementary Fig. 2).

FBR-induced scarring is particularly detrimental to electrical neural interfaces, such as those implanted in nerves. We therefore initially focused on this tissue. Nerve fibroblasts cultured on substrates of varying stiffness for 6 days retained a spherical morphology on soft gels with shear moduli of ~0.1-1 kPa, while cell spreading significantly increased on stiffer substrates with shear moduli of 10-50 kPa (Fig. 1b) (p = 1.2e-7, one-way ANOVA). Adhesion to the substrate via focal adhesions (Fig. 1c) and proliferation (Supplementary Fig. 3) showed similar significant increases with substrate stiffness (adhesion p = 5.2e-9, proliferation p = 0.0023). These observed increases in cell spreading, adhesion, and proliferation are consistent with a fibroblast FBR-like phenotype[30].

Fibroblasts in FBR and other fibrotic processes typically differentiate into myofibroblasts – which are characterised by the expression of alpha smooth muscle actin (αSMA) and high extracellular matrix production[31]. Exposure to the non-physiological high stiffness of 50 kPa significantly increased the synthesis of both αSMA and the extracellular matrix protein collagen I – a primary component of the FBR capsule (Fig. 1d-f) (collagen p = 1.4e-26, αSMA p = 5.3e-26, one-way ANOVAs). Fibronectin - a different extracellular matrix protein – was present in nerve fibroblasts but was largely independent of substrate stiffness (Supplementary Fig. 3) (no significant differences in multiple comparison analysis between 50 kPa and 10 kPa or 0.1 kPa). Our findings are consistent with previous studies in fibroblast populations from other tissues reporting that fibroblasts transition into a myofibroblast phenotype at high substrate stiffnesses[31,32].

Macrophages showed similar functional changes on substrates stiffer than their physiological host tissue. Similar to nerve fibroblasts, cell spreading, adhesion, and proliferation rates were significantly increased if compared to softer substrates (Fig 2a-c, Supplementary Fig. 4) (spreading p = 9.8e-8, adhesion p = 0.009, proliferation p = 0.007, one-way ANOVA). RNA sequencing of macrophages three days post-plating showed significant substrate stiffness-dependent changes in gene expression, particularly in inflammation-related genes

(Fig. 2d), consistent with a switch in phenotype from activated M1 to the anti-inflammatory M2 on stiffer substrates. On 50 kPa substrates, we found downregulation of proinflammatory genes such as interleukin 1 beta (*il1b*) (p = 1.4e-6, FDR adjusted p-value) and prostaglandin E synthase (*ptgs2*) (p = 9.5e-6) in macrophages, while M2-associated genes such as arginase (*arg1*) (p = 0.002) and peroxisome proliferator-activated receptor-γ (*pparγ*) (p = 0.007) were upregulated if compared to soft substrates. This switch to a macrophage M2 activation profile is typically associated with tissue regeneration and fibrosis[33,34]. Together, our *in vitro* experiments indicated that non-physiologically high substrate stiffness may lead to fibrosis, a hallmark of FBR.

Having confirmed that both primary macrophages and nerve fibroblasts assume an FBR-like phenotype when exposed to materials that are stiffer than their host tissues, we sought to test if materials mechanically matched to these tissues may alleviate FBR *in vivo* in rat models. While it is often difficult or impractical to fabricate and use implants made entirely from extremely soft materials because of fabrication and handling challenges, stiff materials can be masked from cells underneath a thick enough layer of a softer material[35–37]. Hence, we designed silicone rubber implants with a shear modulus of ~ 200 kPa which we coated with a 100 μm thick layer of soft material (Fig. 3a) to "stealthen" the underlying stiffer substrate from cells (see Methods for details)[35–37]. The coatings consisted of either soft 0.2 kPa polyacrylamide (PAA_0.2kPa), 2kPa silicone (PDMS_2kPa), or 20 kPa polyacrylamide (PAA_20kPa) (shear moduli, Supplementary Fig. 5). One group of implants remained non-coated (PDMS_200kPa).

These soft-coated devices were implanted first into the subcutaneous space of rats, a common location for medical implants such as pulse generators[38] and biosensors[17]. Three months post-implantation, a time point by which acute inflammation due to implantation has resolved and chronic responses to implanted materials have settled in, FBR was significantly reduced around the implants with soft coatings if compared to the stiffer materials (Fig. 3b)

as revealed by immunohistochemistry. The intensities of markers for myofibroblasts (αSMA), collagen I, and macrophages (CD68) were significantly lower in tissues surrounding soft materials, with greater effects seen at the lowest stiffnesses (Fig. 3c) (αSMA p = 0.005, collagen p = 6.0e-4, CD68 p = 3.4e-5, one-way ANOVAs). Similar to our *in vitro* results, the extracellular matrix protein fibronectin did not vary significantly across groups (Supplementary Fig. 6) (p = 0.14, one-way ANOVA). On the other hand, capsule thickness, a measure of fibroblast proliferation around the implant and of the severity of FBR, was greatly decreased around implants with soft coatings (Fig. 3d, Supplementary Fig. 7) (p = 0.006, one-way ANOVA), suggesting that FBR can be minimized by matching the mechanical properties of the implant surface to those of the surrounding tissue.

To test if the suppression of FBR by implants with soft coatings is a tissue type-specific phenomenon or if it is more generally applicable, we then implanted nerve conduits with or without soft coatings as those described above in a rat model of nerve injury (Fig. 4a) (for details on sciatic nerve transection see Methods). Similar to the subcutaneous implants, intensity of markers for myofibroblasts (αSMA) and macrophages (CD68) were significantly decreased in tissue exposed to the soft coating compared to the non-coated control implants (Fig. 4c) (αSMA p = 0.002, CD68 p = 0.007, one-way ANOVAs). Collagen I also showed a similar trend, although differences were not statistically significant (Fig. 4c) (p = 0.19, one-way ANOVA), while capsules became significantly thinner around softer materials (Fig. 4d) (p = 0.0008, one-way ANOVA), indicating that soft coatings of implants may indeed represent a general approach to alleviate FBR to biomedical implants irrespective of the type of host tissue.

To benchmark the performance of our soft-coated implants against currently used clinical strategies exploiting devices impregnated with chemical repressors[23,24] of inflammatory reactions such as glucocorticoids, we repeated the experiments using implants coated with a ~100 µm thick dexamethasone-impregnated silicone of ~ 200 kPa (Dex)[24]. αSMA,

macrophage, and collagen I levels indicated a similar suppression of FBR in Dex subcutaneous implants and nerve conduits as seen in implants whose coating was similarly soft as the host tissue (Fig. 3c, 4c) ($p > 0.05$ for all stains in both types of implants between PDMS_2kPa & Dex and PAA_0.2kPa & Dex, Bonferroni-corrected Student's t-test). However, as glucocorticoids such as dexamethasone are not only anti-inflammatory but also anti-proliferative, neuronal regeneration was significantly reduced in dexamethasone-doped nerve implants if compared to implants with soft coatings (Fig. 4b, e, Supplementary Fig. 8) ($p = 0.003$, one-way ANOVA). Hence, our data showed that soft coatings of implants not only suppress inflammation and FBR but also permit regeneration – in contrast to currently exploited devices relying on the anti-inflammatory properties of glucocorticoids.

In FBR and fibrosis, the secretion of dense networks of extracellular matrix rich in components such as collagen I leads to an increase in the stiffness of the tissue surrounding the implant[39,40]. To further corroborate the suppression of FBR in tissue surrounding soft coating implants, we used *ex vivo* atomic force microscopy to measure the apparent elastic moduli of tissues exposed to the different implants (Fig. 4f). While, with a median apparent elastic modulus $K \sim 1200$ Pa, tissue around the stiffest conduits showed a large degree of stiffening compared to intact nerve epineurium, tissue around all soft-coated implants showed a low $K \sim 150$ Pa, indistinguishable from dexamethasone-treated controls ($p = 0.70$; Bonferroni-adjusted Student's t-test) and similar in value to intact nerve epineurium ($K = 140$ Pa) (Fig 4g), further indicating that soft implant coatings minimised the development of FBR.

Both our *in vivo* and *in vitro* results indicated that FBR can occur as a consequence of a mechanical mismatch between the native biological tissue and foreign materials. To test if cells indeed responded to the mechanical properties of their environment, we investigated the distribution of the transcriptional regulator YAP in tissue surrounding implants after 3 months. In many systems, YAP is majorly involved in mechanotransduction, i.e., the conversion of mechanical cues into biochemical signals[41]. On soft substrates, YAP is usually excluded from the nucleus, while on stiffer substrates YAP enters the nucleus, leading to

mechanically driven changes in gene expression[42]. This effect has been observed *in vitro* in several cell types including fibroblasts[43] as well as *in vivo*[44]. Immunohistochemical stains indeed revealed a significantly lower nuclear localisation of YAP in tissues exposed to softer coatings if compared to stiffer coatings in both implant types (Fig. 5) (subcutaneous $p = 0.01$, nerve $p = 0.001$, one-way ANOVAs), confirming that cells in the vicinity of medical implants respond to the stiffness of the implant material.

Discussion

Our results are consistent with previous *in vitro* studies showing that cells respond to the stiffness of their environment[7,45–48], and they link this cellular mechanosensitivity to a key problem in medical implants: FBR. Contact with materials stiffer than native tissue leads to trans-differentiation of fibroblasts into myofibroblasts, and macrophages taking on an activated M2-like phenotype, driving tissue generation.

Collectively, our results show that a mechanical mismatch between implant material and host tissue stiffness is a primary driver of FBR, and that this principle can be exploited to minimise FBR by manufacturing mechanically soft implant coatings with a sti□ness similar to the host tissue. Notably, this effect was most pronounced for coatings with shear moduli < 10 kPa, which is orders of magnitude softer than materials commonly used in medical research that are often referred to as “soft implants”[27–29]. This effect was similar for two different soft materials: polyacrylamide and PDMS, and it occurred irrespective of implant design and the location of implantation, indicating a very robust response of host tissues to implant stiffness.

Current medical implants offer a powerful tool for the treatment of a number of clinical conditions. However, long term stability of implants often remains limited by FBR, particularly of those actively interacting with the host’s environment such as electrical neural interfaces.

Corticosteroid drugs such as dexamethasone offer a viable strategy to control FBR in certain situations[23]. However, their anti-inflammatory effect also greatly interferes with regeneration of surrounding tissue[24], making them ill-suited for use in regenerative implants. As shown here, soft coatings offer an effective strategy to minimise FBR without impacting surrounding tissue function or sacrificing the bulk mechanical properties of the implant itself. The coating dimensions and compatibility with existing microfabrication techniques make this technology easily applicable to many implant designs, facilitating translation to the clinic. Moreover, the FBR-reducing effects are linked to the mechanical – and not chemical – properties of the coating materials, providing great flexibility in material choice for different implant designs and applications.

238 *Materials and Methods*

239 **Polyacrylamide cell culture substrates.**

240 Polyacrylamide hydrogels were prepared two days prior to the plating of any cells, using a
241 protocol previously described[49]. 19 mm diameter glass coverslips were cleaned by alternate
242 dipping in ddH_2O and EtOH, and covered in NaOH for 5 min. NaOH was removed, and
243 coverslips were functionalised with APTMS solution for 2.5 min, followed by thorough rinsing
244 in water. Coverslips were finally allowed to sit in a glutaraldehyde 0.5% (v/v) solution in
245 ddH_2O for 30 min at RT.

246 Polyacrylamide premixes were prepared by mixing of acrylamide (40\% w/w; A4058, Sigma),
247 bis-acrylamide (2%; BP1404-250; Fisher Scientific), and hydroxy-acrylamide (97%; 697931;
248 Sigma) solutions (177:100:23 ratio). A volume of PBS was added to the premix to achieve
249 gels of a particular stiffness (Supplementary Table 1). This final gel mix was degassed under
250 a vacuum for 10 min.

251 To initiate polymerisation, 5 µl of ammonium persulfate solution (0.1 g/ml in ddH_2O; Sigma,
252 281778) and 1.5 µl of TEMED (15524-010, Invitrogen) were added to 500 µl of gel mixes. 8
253 µl drops of mix were placed on the treated surface of 19 mm diameter coverslips, and
254 covered with a 22 mm diameter glass coverslip (previously treated with a RainX hydrophobic
255 coating).

256 The gels were allowed to swell in PBS overnight. 22 mm diameter coverslips were then
257 removed to reveal the hydroxyacrylamide gels bound to 19 mm coverslips. These were
258 sterilised under UV light for 1 hour, and functionalised with PDL (100 µg/ml in PBS) at room
259 temperature overnight. Gels used for Schwann cell cultures were further functionalised with
260 laminin (1 µg/ml in PBS) for 2 hours at room temperature. Prior to cell plating, gels were
261 placed in culture medium for 30 min to allow medium to fill them.

***In vitro* assay.** *Nerve fibroblasts.* Cultures were prepared from postnatal day 1 to 5 Sprague Dawley rat sciatic nerves. Using a variation of the procedure previously described[50]. All animal procedures carried out were in compliance with the United Kingdom Animals (Scientific Procedure) Act of 1986 and institutional guidelines.

Sciatic nerves of 10 - 20 animals were dissected out using sterilised microscissors and fine forceps, and were kept in chilled HBSS (14170-112, Invitrogen) to stabilise the pH and osmotic environment. To dissociate the tissue, nerves were transferred to a 2 ml collagenase solution (2 mg/ml; C9407, Sigma) and incubated for 30 min at 37 ºC, after which 2 ml of trypsin (1 mg/ml; T0303, Sigma) was added (20 min, 37 ºC incubation). Finally, 2 ml of deoxyribonuclease (0.1 mg/ml; D5025, Sigma) was added and, after a brief incubation period (2 min), the cells were centrifuged (4 min, 1000 rpm). The supernatant was removed, and the cell pellet was re-suspended in 2 ml of triturating solution (containing 10 mg/ml bovine serum albumin [A7906, Sigma], 0.5 mg/ml trypsin inhibitor [10109886001, Roche], 0.02 mg/ml deoxyribonuclease).

To isolate the population of nerve fibroblasts from the dissociated nerves, the cells were centrifuged and re-suspended in 0.5 ml of DPBS/BSA (Dulbecco's phosphate-buffered saline supplemented with 5 mg/ml bovine serum albumin) and 50 µl of magnetic-bead antibodies against rat/mouse CD90.1 (Thy1.1) (Miltenyi Biotec, 120-094-523) – a marker expressed by nerve fibroblasts[51] - and incubated for 15 min at RT. Cells were centrifuged, re-suspended in 2 ml of chilled DPBS/BSA, and run through a column equipped with a magnetic separator (MiniMACS Separator; Miltenyi Biotec, 130-042-102). Once the buffer had finished running through the column, and the flow-through collected, the column was removed from the magnetic separator, and the magnetically-labelled cells were flushed out with chilled DPBS/BSA. Finally, the positive fraction (nerve fibroblasts) were centrifuged and the cell pellet re-suspended in DMEM (11320-033, Invitrogen) supplemented with a further 4

mM of glutamine (25030032, Invitrogen), 100 mg/ml foetal calf serum (FCS, Invitrogen) and an antibiotic-antimycotic agent (15240-062, Invitrogen). The cells were plated on polyacrylamide substrates at a density of 10,000 cells/cm^2.

Bone marrow-derived macrophages. Macrophages were derived from adult rat bone marrow hematopoietic stem cells as previously described[52]. Adult Sprague Dawley rats were sacrificed by exposure to a rising concentration of CO_2. The femurs were dissected out and broken open using sterile scissors. Bone marrow contained within the femurs was washed out with chilled DPBS and collected. The cell suspension was centrifuged for 10 min at 1000 rpm. The supernatant was discarded and the cells were re-suspended in BMDM (the same supplemented DMEM used for nerve fibroblasts, further supplemented with macrophage colony stimulating factor [400-28, Peprotech; 50 ng/ml]). Cells were counted in a hemocytometer and seeded on 100 x 15 mm uncoated petri dishes (Sigma, P5731) at a density of 5,000 cells/cm^2. The dishes were supplemented with further medium after 3 days of culture at 37 ºC.

Hematopoietic stem cells differentiate into macrophages in the presence of macrophage colony stimulating factor present in BMDM. After 6 days to allow differentiation of Hematopoietic stem cells differentiate into macrophages, the medium in the dishes was removed to dispose of any cells which had not attached to the substrate. The remaining cells were washed with warm DPBS followed by CellStripper solution (Corning, 25-056-CI). Cells were incubated in CellStripper for 5 min at 37 ºC to detach them from the substrate. The cell suspension was collected and an equal volume of BMDM was added to inactivate the CellStripper solution. Cells were then centrifuged at 1000 rpm for 10 min and the supernatant was removed. Upon re-suspension in BMDM and counting, cells were plated onto polyacrylamide substrates at a density of 10,000 cells/cm^2.

Immunocytochemistry.

Cell stains were carried out 6 days after plating on polyacrylamide substrates. At this point in time, warm paraformaldehyde solution (40 mg/ml in PBS) was added to the cells for 15 min at room temperature. The fixative solution was washed off with PBS (3 washes, 10 min per wash). To improve antibody specificity cells were incubated for 30 min at room temperature in a blocking solution consisting of 0.03% v/v Triton X-100 (Sigma, T8787) and 3% v/v bovine serum albumin (Sigma, A9418) in PBS. Primary antibodies (in blocking buffer) were then added to cells and incubated overnight at 4 °C. Further details regarding antibody concentrations can be found in Supplementary Table 2.

Excess primary antibodies were washed off using PBS (3 washes, 10 min). Secondary antibodies in blocking buffer were incubated on the cells for 2 hr at room temperature. Following a wash with non-saline Tris-buffered solution, Fluorsave mounting agent (Millipore, 345789) was added to sections to preserve fluorescence before gels were placed onto glass slides and stored at 4 °C prior to imaging.

Imaging of stained cells on polyacrylamide substrates was carried out using a confocal microscope (Leica TCS SP5). For every condition 3 images were taken at random sites within each gel. The nuclear stain was used as a guide to ensure cells were present in the field of view when pictures were taken. Gain and exposure settings for each channel used were maintained constant between imaging sessions and across different stains.

Cell counts were performed by hand in the Image-J software package (v1.48, National Institutes of Health, USA). Contrast of images was modified prior to analysis. For morphological stains, one image of high stiffness (50 kPa) and one of low stiffness (0.1 kPa) were opened and their contrast modified to an equal degree until a satisfactory pattern of stain was achieved in both. This contrast modification was then applied to all images of the same batch of stained gels. For cell-type specific stains such as alpha-smooth muscle actin this same contrast modification was carried out using negative and positive control stains.

Cells were counted, or the area stained was designated, by hand. Statistical analysis and data plotting was carried out using MATLAB (Mathworks, R2016b).

RNA sequencing.

RNA sequencing was performed in parallel on n = 4 biological replicates. RNA extraction was carried out at day 3 of culture on polyacrylamide substrates using an RNeasy Plus Micro Kit (Qiagen, 74034). Prior to and at regular intervals during the extraction procedure, work surfaces and pipettes were cleaned with RNase Zap decontamination solution (ThermoFisher, AM9780) to inactivate RNases and prevent sample RNA degradation. To collect the cells, each coverslip was briefly washed in PBS and lifted out of the solution using forceps. The gels onto which the cells were attached were gently scraped off from the coverslips using a sterile steel blade and placed in RLT lysis buffer plus (Qiagen). The samples in buffer were then moved to QIAshredder tubes (Qiagen, 79654) and centrifuged in a microcentrifuge (MSE, mistral 1000) for 2 min at 8,000g. Instructions provided by the kit manufacturer were then followed to extract cellular RNA, which was collected and stored at -80°C.

RNA quantification and integrity analysis were carried out on all samples prior to library preparation. Using an RNA 6000 Pico Kit (Agilent, 5067-1513), samples concentration and integrity was analysed using an Agilent 2100 Bioanalyzer. No samples with an RNA integrity number <7 were used. Library preparation was thereafter carried out using an Ovation RNA-Seq System V2 kit (NuGen, 7102-32), following manufacturer instructions. Samples were finally submitted for sequencing in an Illumina HiSeq 2500 system.

Illumina read data files were run through a bioinformatics pipeline and aligned with the *Rattus norvegicus* genome (Ensembl Rnor_6.0). Fold changes and p-values were calculated for each gene between each experimental group and a control group (consisting of the

364 combined 0.1 kPa and 1 kPa conditions). Genes expressed were filtered to produce lists of
365 differentially expressed genes (DEGs). Defined by a minimum of 2-fold change in
366 expression, a base expression above 3 normalised counts, and an adjusted p-value below
367 0.05. Principal component analysis was carried out on data from these experiments
368 (Supplementary Fig. 9). RNAseq data have been deposited in the ArrayExpress database at
369 EMBL-EBI (https://www.ebi.ac.uk/arrayexpress/experiments/E-MTAB-7900) under accession
370 number E-MTAB-7900. Code to create the figures displaying RNAseq results is available in
371 the following GitHub repository: https://github.com/CTR-BFX/2019-Carnicer-Lombarte.

372

373 **Implant fabrication.**

374 *Nerve conduits.* Moulds of the cuff implants were designed in 3D-CAD software (AutoCAD,
375 Autodesk Inc) and 3D printed in PLA (polylactic acid) plastic using a MakerGear M2 3D
376 printer (MakerGear). The moulds were covered in Sylgard 184 PDMS, and were placed in an
377 oven at 65°C overnight. The 3D printed mould was removed from the cured PDMS,
378 producing a negative pattern of the cuff implants. The surface of the PDMS negative moulds
379 was activated using oxygen plasma (Diener plasma etcher) for 25 seconds at 30 W, and 0.8
380 mbar chamber pressure. PDMS moulds were then functionalised using
381 Trichloro(1H,1H,2H,2H-perfluorooctyl)silane (Sigma, 448931). A few drops of silane were
382 placed on a glass petri dish and into a desiccator together with the PDMS moulds. The
383 desiccator was pumped down into a vacuum, and functionalisation was allowed to take place
384 overnight. The resulting layer of silane prevented any new PDMS cured on these moulds
385 from binding to them, allowing for the casting of the PDMS cuffs from these negative moulds.

386 To cast the cuffs, flat petri dishes with raised edges were prepared. These edges were
387 produced through layering multiple layers of insulation PVC tape, until a thickness of 0.6 mm
388 was achieved. The functionalised PDMS negative moulds were coated with a thick layer of
389 Sylgard 184 PDMS and placed on top of these dishes. The raised edges of the dishes

created a 0.6 mm thick layer of Sylgard 184 PDMS below the moulds, which would become part of the cuffs after curing. The moulds and dishes were placed in an oven at 65°C overnight.

The freshly-cured layer of PDMS was carefully peeled from the moulds and trimmed to the appropriate dimensions with a steel blade. The resulting PDMS implants were functionalised with an additional layer of silicone/polyacrylamide before rolling into cuffs. To roll into cuffs, the edges of the implants were brought together and carefully secured with insulation PVC tape. The edges were covered with RTV PDMS (SA03073, Farnell), which was allowed to cure overnight. An additional layer of RTV was then added and allowed to cure before the cuffs were stored in PBS and sterilised under UV prior to implantation. The resulting conduit had a length of 7 mm, an internal diameter of 1.5 mm, and a wall thickness of 0.6 mm.

Subcutaneous implants. A 3 mm thick layer of Sylgard 184 PDMS was cast and cured overnight at 65 ºC. This was then trimmed using a steel blade into 5 x 5 mm blocks. Each block then was functionalised with a coating. Four blocks – one for each of the 4 stiffness-controlled conditions – were combined into one 10 x 10 mm implant and stuck together using RTV silicone. The sides of each of the four component blocks were notched to later be able to identify them. Dexamethasone-doped implants remained as 5 x 5 mm blocks, and were not combined with other implants. Implants were stored in PBS and sterilised under UV prior to implantation.

Coatings. To produce dexamethasone-doped silicone implants (Dex), Sylgard 184 PDMS was doped with 10 mg/ml of dexamethasone and spin-coated into 100 µm-thick films. The dexamethasone-doped films were cut into appropriately-sized rectangles. A small amount of RTV PDMS was spread over an implant and a dexamethasone-doped PDMS rectangle was placed on top. After allowing the RTV to cure overnight, the dexamethasone-doped film was further trimmed of any overhangs and the PDMS cuff was rolled as described above.

Soft silicone coatings (PDMS_2kPa) were prepared from a mix of NuSil 8100 and Sylgard 184 (99% to 1% w/w, respectively). An implant was thoroughly cleaned with ethanol and ddH_2O and dried with nitrogen gas, followed by the application of a 9 µl drop of the soft silicone mix to its surface. This drop was spread out to ensure that the entire inner surface of the implant was completely covered. The implant was then transferred to an oven and baked at 65 °C for one week. This long curing time was a necessary step to remove traces of non-cured PDMS.

Polyacrylamide coatings (PAA_0.2kPa and PAA_20kPa) were grafted onto Sylgard 184 PDMS implants following a published protocol[53].Glass coverslips were cleaned by alternate dipping in ddH_2O and EtOH. PDMS implants were thoroughly cleaned with methanol, dried with nitrogen gas, and covered with a benzophenone solution 10% w/w in EtOH (Sigma, B9300) for 2 min at room temperature. Benzophenone was removed and cuffs cleaned with methanol and dried with nitrogen gas. Polyacrylamide hydrogel mixes were prepared by combining acrylamide and bisacrylamide solutions at a 2:1 ratio. The mixes were combined with PBS to achieve the desired stiffness, as described in Supplementary Table 1. To initiate the polymerisation of the gel mix, 5 µl of APS solution (0.1 g/ml in ddH_2O) and 1.5 µl of TEMED were added to 500 µl of gel mixes. A 9 µl drop of the gel mix was then transferred to a PDMS implant, which had been previously soaked in 10% (w/w) benzophenone solution in ethanol. The drops were spread out by covering with a clean glass coverslip. Implants were then quickly transferred under a 12 J/cm^2 UV lamp for 10 min (SUSS MicroTec MJB4). After the 10 min of UV exposure, glass coverslips were removed and polyacrylamide-PDMS composites were placed in PBS for a further 30 min. The polyacrylamide coating was kept hydrated with PBS at all times until implantation.

Stiff silicone implants (PDMS_200kPa) were not coated with anything, leaving the surface of the Sylgard 184 implant exposed to the tissue.

441 ***In vivo* implantation.**

442 All experimental procedures were performed in accordance with the UK Animals (Scientific
443 Procedures) Act 1986. Surgical procedures were carried out under aseptic conditions. ~250
444 g Lewis rats (Charles River UK) were housed in groups of 5 and provided *ad libitum* access
445 to food and water for a minimum of 7 days prior to surgical procedures. Immediately prior to
446 all surgical procedures, animals received an injectable dose of the non-steroidal anti-
447 inflammatory drug meloxicam (1.5 mg/ml, subcutaneous). Anaesthesia was induced and
448 maintained with isoflurane delivered via a facemask. Body temperature was monitored via a
449 rectal probe and maintained at 37 °C using a thermal blanket.

450 *Nerve conduits.* Biceps femoris and vastus lateralis muscles of the right leg of the animals
451 were approached dorsally and separated to expose the septum through which the sciatic
452 nerve travels. The sciatic nerve trifurcation point was located and followed 2 mm proximal.
453 This site was used as a landmark to achieve consistent location of injury or implantation. The
454 nerve was cleanly transected at this location using scissors and the conduit was positioned
455 between the two resulting nerve stumps, leaving a 5 mm long empty gap within the conduit
456 between the stumps. The epineurium of each nerve stump was sutured to the silicone tube
457 using 9/0 nylon sutures (Ethicon). Each animal received only one conduit, with a single type
458 of coating.

459 *Subcutaneous implants.* An incision was done dorsally over the right leg of an animal
460 (approximately above the femur). The skin was separated from the underlying muscle using
461 blunt forceps to create a tunnel from the site of incision towards the midline of the animal.
462 The implant was fed through this tunnel and placed ~1 cm away from the midline, with the
463 coating facing the layer of muscle. Each animal received one subcutaneous implant; either a
464 composite stiffness or a dexamethasone-doped implant.

All animals were allowed to recover following implantation. A further dose of meloxicam was given orally the day after surgery. 3 months post-implantation, animals were sacrificed by exposure to a rising concentration of CO_2 and the tissue collected.

Immunohistochemistry.

All tissue was fixed prior to processing and staining by immersion in paraformaldehyde solution (40 mg/ml in PBS) overnight at 4 °C. Samples which required sectioning were then transferred to a sucrose solution (30% w/w in PBS) for cryoprotection. They were kept in this solution for a minimum of 16 hr at 4 °C, and then stored until further processing. Cryopreserved samples were embedded in optimal cutting temperature compound (Tissue-Tek, 4583), which was frozen and mounted on a cryostat (CM3050 S, Leica). 12 μm - thick sections were cut from the samples at a cutting temperature of -20 °C. Sections were placed on glass slides and allowed to dry at room temperature overnight before storage at -20 °C until stained.

Sections ready to be stained were washed in a Triton X-100 0.1% v/v solution in PBS to or permeabilisation. These and all further washes were performed three times for 10 min. To minimise non-specific antibody binding, sections were incubated in a blocking buffer, consisting of tris-buffered saline containing 0.03% v/v Triton X-100 and 10% v/v donkey serum (Millipore, s30-100ml). After blocking for 1 hr at room temperature, primary antibodies were added to sections (further details in Supplementary Table 2). Sections were covered with paraffin film to prevent drying and were incubated in primary antibodies overnight at 4 °C.

Sections were washed in PBS-Triton solution to remove excess primary antibodies, and then incubated in secondary antibodies in blocking buffer for 2 hr at room temperature. Secondary antibodies were finally washed off with a non-saline Tris-buffered solution.

Fluorsave mounting agent (Millipore, 345789) was added to sections to preserve fluorescence before encasing with a glass coverslip and storing at 4 °C prior to imaging.

Imaging of stained nerve tissue was carried out using a confocal microscope (Leica TCS SP5). Image files were exported and processed for analysis in Image-J software package (v1.48, National Institutes of Health, USA). Stain intensity profiles of FBR capsules was carried out through a combination of custom Matlab and Fiji scripts. The edge of the nerve capsule was delineated by the user and aligned by the scripts. An intensity profile (intensity vs. depth into the nerve) of the each stain was obtained. The average intensity from the edge of the nerve to a depth of 25 μm was calculated and provided as a ratio to the same intensity of the PDMS_200kPa group. The only exception were CD68 stains, were a depth of 50 μm was instead chosen as macrophages were found to mostly locate deeper into the tissue than other markers. Capsule thickness was using a Matlab script, after its edge was marked by hand based on the αSMA stain. Axon density was analysed in an automated fashion using a Fiji script over 3 randomly chosen 100 x 100 μm boxes for every image. Statistical analysis and data plotting was carried out using MATLAB (Mathworks, R2016b).

Atomic force microscopy.

Sample elasticity was determined via atomic force microscopy (AFM) as previously described[54]. Indentation measurements using a cantilever probe were taken on samples placed on an inverted optical microscope (Axio Observer.A1, Carl Zeiss Ltd.) using a JPK Nanowizard Cellhesion 200 AFM (JPK Instruments AG). Tipless silicon cantilevers (Arrow-TL1; NanoSensors) with a spring constant of ~0.02 N/m were used in experiments were tissue stiffness was measured. Material characterisation made use of either these or stiffer cantilevers (SICON-TL-20, spring constant ~0.29 N/m, AppNano; TL-FM-10, spring constant ~2.8 N/m; Nanosensors; spring constant value calculated via the thermal noise method[55]).

Each cantilever had a polystyrene bead (~37 μm diameter for tissue, ~20μm for stiffer materials; Microparticles GmbH) glued (ultraviolet curing, Loctite) prior to all measurements.

Tissue preparation. Lewis rats (Charles River UK) were sacrificed by overdose of euthatal (pentobarbitone) administered intraperitoneally, followed by neck dislocation. Euthatal was combined at a 1:1 v/v ratio with lidocaine anaelgesic and delivered at a total dose of 3 ml/kg of bodyweight. Further processing of tissue was carried out within 1 - 2 hr of animal sacrifice, and all AFM measurements were completed within 5 hr to minimise tissue degradation.

To dissect out the sciatic nerve, the dorsal side of the hindlegs was exposed and skin removed. Biceps femoris and vastus lateralis muscles were separated to expose the septum through which the sciatic nerve travels. The nerve was dissected out and transected just below the trifurcation point, and 1 cm above it. The nerve was then transferred to a dish containing mammalian physiological saline previously described by others[56] (121 mM NaCl, 5 mM KCl, 1 mM $MgCl_2$, 1 mM $CaCl_2$, 0.4 mM NaH_2PO_4, 23.8 mM $NaHCO_3$, 5.6 mM glucose). Mammalian physiological saline was prepared freshly prior to the experiment. To establish a pH of 7.3, a gas mixture of 95% CO_2 and 5% O_2 was bubbled through the solution.

For naïve nerve measurements, under a dissection microscope, blood vessels and excess tissue surrounding the nerve were removed, and the nerve stumps were trimmed off with a steel blade. The remaining nerve was then cut into several fragments for mounting and sectioning. Nerve fragments were embedded in warm 4% w/w low melting point agarose (Sigma) in PBS. Agarose was allowed to cool and harden for a few minutes before trimming into blocks containing the nerve fragments. Blocks were stuck to a steel stage with cyanoacrylate glue and transferred to a chamber filled with chilled mammalian physiological saline. The blocks were cut into 500 μm thick sections in a vibrating microtome. Nerve sections were transferred to mammalian physiological saline solution containing the live stain fluoromyelin (1:250 v/v in mammalian physiological saline; Invitrogen, F34651) and

incubated for 1 hr at room temperature to stain the myelin surrounding axons. This allowed the endoneurial compartment to be identified and later probed via AFM. Sections were mounted onto 35 mm plastic dishes (Z707651, Sigma). The sections were gently deposited onto two strips of cyanoacrylate glue which adhered to the agarose on which the tissue was embedded. Dishes were filled with room temperature mammalian phosphate buffer and transferred to the inverted microscope to perform the measurements.

For nerve FBR capsules and epineurium measurements, implanted cuffs were extracted from rats 3 months post-implantation with regenerated sciatic nerves still within them. Under a dissection microscope, fibrotic tissue covering the outside of cuffs was removed. A cut was done along the length of the cuff, and the regenerated nerve fragment within was carefully removed. The nerve fragment was embedded on its side on a shallow bed of 4% w/w low melting point agarose (Sigma), and submerged in mammalian physiological saline. Finally, AFM measurements of the side of the nerve were carried out.

Material preparation. The stiffness of polyacrylamide hydrogel and silicone rubber implants and substrates was checked for every manufactured batch by AFM. Implants and substrates were all cleaned by immersion in PBS overnight. These were then transferred to 35 mm plastic dishes and fixed in place using a small amount of vaseline petroleum jelly. Dishes were transferred to the inverted microscope to perform AFM measurements.

Indentation experiments. Petri dishes containing the samples to be analysed were placed on a motorised xy stage, which allowed movement of the sample relative to the AFM cantilever. A CCD camera (The Imaging Source GmbH) was used to image and track the position of the cantilever above the sample. This setup was used to locate and define an area of interest on the sample on which AFM measurements were taken. A custom python script broke down this area into 20 x 20 μm squares, inside which a single measurement was taken. The motorised stage was moved as measurements were taken to perform a raster scan of the area of interest.

For each elasticity measurement, the cantilever probe was lowered onto the surface of the sample at a speed of 10 μm/s. Upon contact and indentation of the sample, the probe continued to be lowered until a force of 10 nN was reached (usually equivalent to an indentation depth δ of 1 to 5 μm). The probe was then retracted, the sample moved, and a measurement repeated at a different location.

The force-distance measurements taken by the AFM were translated into elasticity values using the Hertz model[57] using a previously described custom[58] MATLAB (Mathworks, R2008a) script. for every indentation of the sample. The cantilever and polystyrene bead probe on the sample was modelled as a sphere and a half space, and used to calculate the apparent reduced elastic modulus *K*.

$$F = \frac{4}{3} K R^{\frac{1}{2}} \delta^{\frac{3}{2}}$$

With *F* being the force applied and R the radius of the polystyrene bead. Elasticity was calculated at an indentation depth δ of 2 mm. The reduced elastic modulus may be further transformed into other elastic moduli, including Young's modulus (*E*)[58] and Shear modulus (*G*). A Poisson ratio ν of polyacrylamide was set to 0.48[59], while for PDMS a value of 0.499 was used[60].

$$K = \frac{E}{1 - \nu^2}$$

$$G = \frac{E}{2(1 + \nu)}$$

583 **References**

584 1. Salatino, J. W., Ludwig, K. A., Kozai, T. D. Y. & Purcell, E. K. Glial responses to implanted electrodes
585 in the brain. *Nat. Biomed. Eng.* **1**, 862–877 (2017).
586 2. Spearman, B. S. *et al.* Tissue-Engineered Peripheral Nerve Interfaces. *Adv. Funct. Mater.* **28**,
587 1701713 (2018).
588 3. Kenneth Ward, W. A Review of the Foreign-body Response to Subcutaneously-implanted Devices:
589 The Role of Macrophages and Cytokines in Biofouling and Fibrosis. *J. Diabetes Sci. Technol. Online*
590 **2**, 768–777 (2008).
591 4. Veiseh, O., Tang, B. C., Whitehead, K. A., Anderson, D. G. & Langer, R. Managing diabetes with
592 nanomedicine: challenges and opportunities. *Nat. Rev. Drug Discov.* **14**, 45–57 (2015).
593 5. Anderson, J. M., Rodriguez, A. & Chang, D. T. Foreign body reaction to biomaterials. *Semin.*
594 *Immunol.* **20**, 86–100 (2008).
595 6. Bryers, J. D., Giachelli, C. M. & Ratner, B. D. Engineering biomaterials to integrate and heal: The
596 biocompatibility paradigm shifts. *Biotechnol. Bioeng.* **109**, 1898–1911 (2012).
597 7. Moshayedi, P. *et al.* The relationship between glial cell mechanosensitivity and foreign body
598 reactions in the central nervous system. *Biomaterials* **35**, 3919–3925 (2014).
599 8. Liu, Y. *et al.* Soft and elastic hydrogel-based microelectronics for localized low-voltage
600 neuromodulation. *Nat. Biomed. Eng.* **3**, 58 (2019).
601 9. Jansen, L. E. *et al.* Zwitterionic PEG-PC hydrogels modulate the foreign body response in a
602 modulus-dependent manner. *Biomacromolecules* **19**, 2880–2888 (2018).
603 10. Spencer, K. C. *et al.* Characterization of Mechanically Matched Hydrogel Coatings to Improve
604 the Biocompatibility of Neural Implants. *Sci. Rep.* **7**, 1–16 (2017).
605 11. Brindley, G. S., Polkey, C. E. & Rushton, D. N. Sacral anterior root stimulators for bladder
606 control in paraplegia. *Paraplegia* **20**, 365–381 (1982).
607 12. Anderson, W. S. & Lenz, F. A. Surgery Insight: deep brain stimulation for movement
608 disorders. *Nat. Rev. Neurol.* **2**, 310–320 (2006).

609 13. Proctor, C. M. *et al.* Electrophoretic drug delivery for seizure control. *Sci. Adv.* **4**, (2018).

610 14. Feiner, R. *et al.* Engineered hybrid cardiac patches with multifunctional electronics for online
611 monitoring and regulation of tissue function. *Nat. Mater.* **15**, 679–685 (2016).

612 15. Khodagholy, D. *et al.* NeuroGrid: recording action potentials from the surface of the brain.
613 *Nat. Neurosci.* **18**, 310–315 (2015).

614 16. Yang, X. *et al.* Bioinspired neuron-like electronics. *Nat. Mater.* 1 (2019). doi:10.1038/s41563-
615 019-0292-9

616 17. Chew, D. J. *et al.* A Microchannel Neuroprosthesis for Bladder Control After Spinal Cord
617 Injury in Rat. *Sci. Transl. Med.* **5**, 210ra155-210ra155 (2013).

618 18. Doloff, J. C. *et al.* Colony stimulating factor-1 receptor is a central component of the foreign
619 body response to biomaterial implants in rodents and non-human primates. *Nat. Mater.* **16**, 671–
620 680 (2017).

621 19. Dondossola, E. *et al.* Examination of the foreign body response to biomaterials by nonlinear
622 intravital microscopy. *Nat. Biomed. Eng.* **1**, 0007 (2017).

623 20. Veiseh, O. *et al.* Size- and shape-dependent foreign body immune response to materials
624 implanted in rodents and non-human primates. *Nat. Mater.* **14**, 643–651 (2015).

625 21. Bochenek, M. A. *et al.* Alginate encapsulation as long-term immune protection of allogeneic
626 pancreatic islet cells transplanted into the omental bursa of macaques. *Nat. Biomed. Eng.* **2**, 810–
627 821 (2018).

628 22. Xie, X. *et al.* Reduction of measurement noise in a continuous glucose monitor by coating the
629 sensor with a zwitterionic polymer. *Nat. Biomed. Eng.* **2**, 894–906 (2018).

630 23. Mond, H. G., Helland, J. R., Stokes, K., Bornzin, G. A. & McVENES, R. The Electrode-Tissue
631 Interface: The Revolutionary Role of Steroid-Elution. *Pacing Clin. Electrophysiol.* **37**, 1232–1249
632 (2014).

633 24. FitzGerald, J. J. Suppression of scarring in peripheral nerve implants by drug elution. *J. Neural*
634 *Eng.* **13**, 026006 (2016).

635 25. Franze, K., Janmey, P. A. & Guck, J. Mechanics in Neuronal Development and Repair. *Annu.*
636 *Rev. Biomed. Eng.* **15**, 227–251 (2013).
637 26. Cox, T. R. & Erler, J. T. Remodeling and homeostasis of the extracellular matrix: implications
638 for fibrotic diseases and cancer. *Dis. Model. Mech.* **4**, 165–178 (2011).
639 27. Minev, I. R. *et al.* Electronic dura mater for long-term multimodal neural interfaces. *Science*
640 **347**, 159–163 (2015).
641 28. Lacour, S. P., Courtine, G. & Guck, J. Materials and technologies for soft implantable
642 neuroprostheses. *Nat. Rev. Mater.* **1**, 16063 (2016).
643 29. Capogrosso, M. *et al.* Advantages of soft subdural implants for the delivery of
644 electrochemical neuromodulation therapies to the spinal cord. *J. Neural Eng.* **15**, 026024 (2018).
645 30. Damanik, F. F. R., Rothuizen, T. C., van Blitterswijk, C., Rotmans, J. I. & Moroni, L. Towards an
646 in vitro model mimicking the foreign body response: tailoring the surface properties of
647 biomaterials to modulate extracellular matrix. *Sci. Rep.* **4**, 6325 (2014).
648 31. Hinz, B. *et al.* The Myofibroblast. *Am. J. Pathol.* **170**, 1807–1816 (2007).
649 32. Santoro, R. *et al.* Activation of human aortic valve interstitial cells by local stiffness involves
650 YAP-dependent transcriptional signaling. *Biomaterials* **181**, 268–279 (2018).
651 33. Brown, B. N., Ratner, B. D., Goodman, S. B., Amar, S. & Badylak, S. F. Macrophage
652 polarization: An opportunity for improved outcomes in biomaterials and regenerative medicine.
653 *Biomaterials* **33**, 3792–3802 (2012).
654 34. Hesketh, M., Sahin, K. B., West, Z. E. & Murray, R. Z. Macrophage Phenotypes Regulate Scar
655 Formation and Chronic Wound Healing. *Int. J. Mol. Sci.* **18**, (2017).
656 35. Engler, A. J., Sen, S., Sweeney, H. L. & Discher, D. E. Matrix Elasticity Directs Stem Cell
657 Lineage Specification. *Cell* **126**, 677–689 (2006).
658 36. Kuo, C.-H. R., Xian, J., Brenton, J. D., Franze, K. & Sivaniah, E. Complex Stiffness Gradient
659 Substrates for Studying Mechanotactic Cell Migration. *Adv. Mater.* **24**, 6059–6064 (2012).

660 37. Choi, Y. S. *et al.* The alignment and fusion assembly of adipose-derived stem cells on
661 mechanically patterned matrices. *Biomaterials* **33**, 6943–6951 (2012).
662 38. Bardy, G. H. *et al.* An Entirely Subcutaneous Implantable Cardioverter–Defibrillator. *N. Engl.*
663 *J. Med.* **363**, 36–44 (2010).
664 39. Georges, P. C. & Janmey, P. A. Cell type-specific response to growth on soft materials. *J.*
665 *Appl. Physiol.* **98**, 1547–1553 (2005).
666 40. Swift, J. *et al.* Nuclear Lamin-A Scales with Tissue Stiffness and Enhances Matrix-Directed
667 Differentiation. *Science* **341**, 1240104 (2013).
668 41. Dupont, S. *et al.* Role of YAP/TAZ in mechanotransduction. *Nature* **474**, 179–183 (2011).
669 42. Elosegui-Artola, A. *et al.* Force Triggers YAP Nuclear Entry by Regulating Transport across
670 Nuclear Pores. *Cell* **171**, 1397-1410.e14 (2017).
671 43. Calvo, F. *et al.* Mechanotransduction and YAP-dependent matrix remodelling is required for
672 the generation and maintenance of cancer-associated fibroblasts. *Nat. Cell Biol.* **15**, 637–646
673 (2013).
674 44. Pocaterra, A. *et al.* F-actin dynamics regulates mammalian organ growth and cell fate
675 maintenance. *J. Hepatol.* (2019). doi:10.1016/j.jhep.2019.02.022
676 45. Discher, D. E., Janmey, P. & Wang, Y. Tissue Cells Feel and Respond to the Stiffness of Their
677 Substrate. *Science* **310**, 1139–1143 (2005).
678 46. Trepat, X. *et al.* Universal physical responses to stretch in the living cell. *Nature* **447**, 592–
679 595 (2007).
680 47. Wirtz, D., Konstantopoulos, K. & Searson, P. C. The physics of cancer: the role of physical
681 interactions and mechanical forces in metastasis. *Nat. Rev. Cancer* **11**, 512–522 (2011).
682 48. Discher, D. *et al.* Biomechanics: Cell Research and Applications for the Next Decade. *Ann.*
683 *Biomed. Eng.* **37**, 847 (2009).
684 49. Moshayedi, P. *et al.* Mechanosensitivity of astrocytes on optimized polyacrylamide gels
685 analyzed by quantitative morphometry. *J. Phys. Condens. Matter* **22**, 194114 (2010).

686 50. Brockes, J. P., Fields, K. L. & Raff, M. C. Studies on cultured rat Schwann cells. I.
687 Establishment of purified populations from cultures of peripheral nerve. *Brain Res.* **165**, 105–118
688 (1979).
689 51. Richard, L., Védrenne, N., Vallat, J.-M. & Funalot, B. Characterization of Endoneurial
690 Fibroblast-like Cells from Human and Rat Peripheral Nerves. *J. Histochem. Cytochem.* **62**, 424–435
691 (2014).
692 52. Lynn, A. D. & Bryant, S. J. Phenotypic Changes in Bone Marrow Derived Murine Macrophages
693 cultured on PEG-based Hydrogels and Activated by Lipopolysaccharide. *Acta Biomater.* **7**, 123–
694 132 (2011).
695 53. Yuk, H., Zhang, T., Parada, G. A., Liu, X. & Zhao, X. Skin-inspired hydrogel–elastomer hybrids
696 with robust interfaces and functional microstructures. *Nat. Commun.* **7**, 12028 (2016).
697 54. Koser, D. E., Moeendarbary, E., Hanne, J., Kuerten, S. & Franze, K. CNS Cell Distribution and
698 Axon Orientation Determine Local Spinal Cord Mechanical Properties. *Biophys. J.* **108**, 2137–2147
699 (2015).
700 55. Hutter, J. & Bechhoefer, J. Calibration of Atomic-Force Microscope Tips. *Rev. Sci. Instrum.* **64**,
701 1868–1873 (1993).
702 56. Brown, R. *et al.* Activity-dependent degeneration of axotomized neuromuscular synapses in
703 WldS mice. *Neuroscience* **290**, 300–320 (2015).
704 57. Hertz, H. Ueber die Berührung fester elastischer Körper. *J. Für Reine Angew. Math.* **92**, 156–
705 171 (1882).
706 58. Gautier, H. O. B. *et al.* Chapter 12 - Atomic force microscopy-based force measurements on
707 animal cells and tissues. in *Methods in Cell Biology* (ed. Paluch, E. K.) **125**, 211–235 (Academic
708 Press, 2015).
709 59. Boudou, T., Ohayon, J., Picart, C. & Tracqui, P. An extended relationship for the
710 characterization of Young's modulus and Poisson's ratio of tunable polyacrylamide gels.
711 *Biorheology* **43**, 721–728 (2006).

712 60. Johnston, I. D., McCluskey, D. K., Tan, C. K. L. & Tracey, M. C. Mechanical characterization of
713 bulk Sylgard 184 for microfluidics and microengineering. *J. Micromechanics Microengineering* **24**,
714 035017 (2014).

715

716 **Acknowledgements**

717 The authors would like to thank Jessica Kwok for technical support and advice. Part of the
718 RNA-Seq work was performed with the Genomics and Transcriptomics Core, which is
719 funded by the UK Medical Research Council (MRC) Metabolic Disease Unit
720 (MRC_MC_UU_12012/5) and a Wellcome Trust Major Award (208363/Z/17/Z), and
721 guidance from Marcella Ma, whom the authors wish to thank. This work was furthermore
722 supported by the UK Medical Research Council (MRC) and the Sackler Foundation (doctoral
723 training grant RG70550 to ACL), the UK Wellcome Trust (Translational Medicine and
724 Therapeutics PhD Programme Fellowship 109511/Z/15/Z to DGB), the Centre for
725 Trophoblast Research (MP and RSH), the Whitaker International Scholars Program (ALR),
726 the European Commission's Horizon 2020 (Marie Sklodowska-Curie Fellowship 797506 to
727 ALR), the Bertarelli Foundation (SPL), the European Research Council (Consolidator Award
728 772426 to KF), the UK Biotechnology and Biological Sciences Research Council (Research
729 Grant BB/N006402/1 to KF), and the UK Medical Research Council (Career Development
730 Award G1100312/1 to KF).

731

732 **Figures**

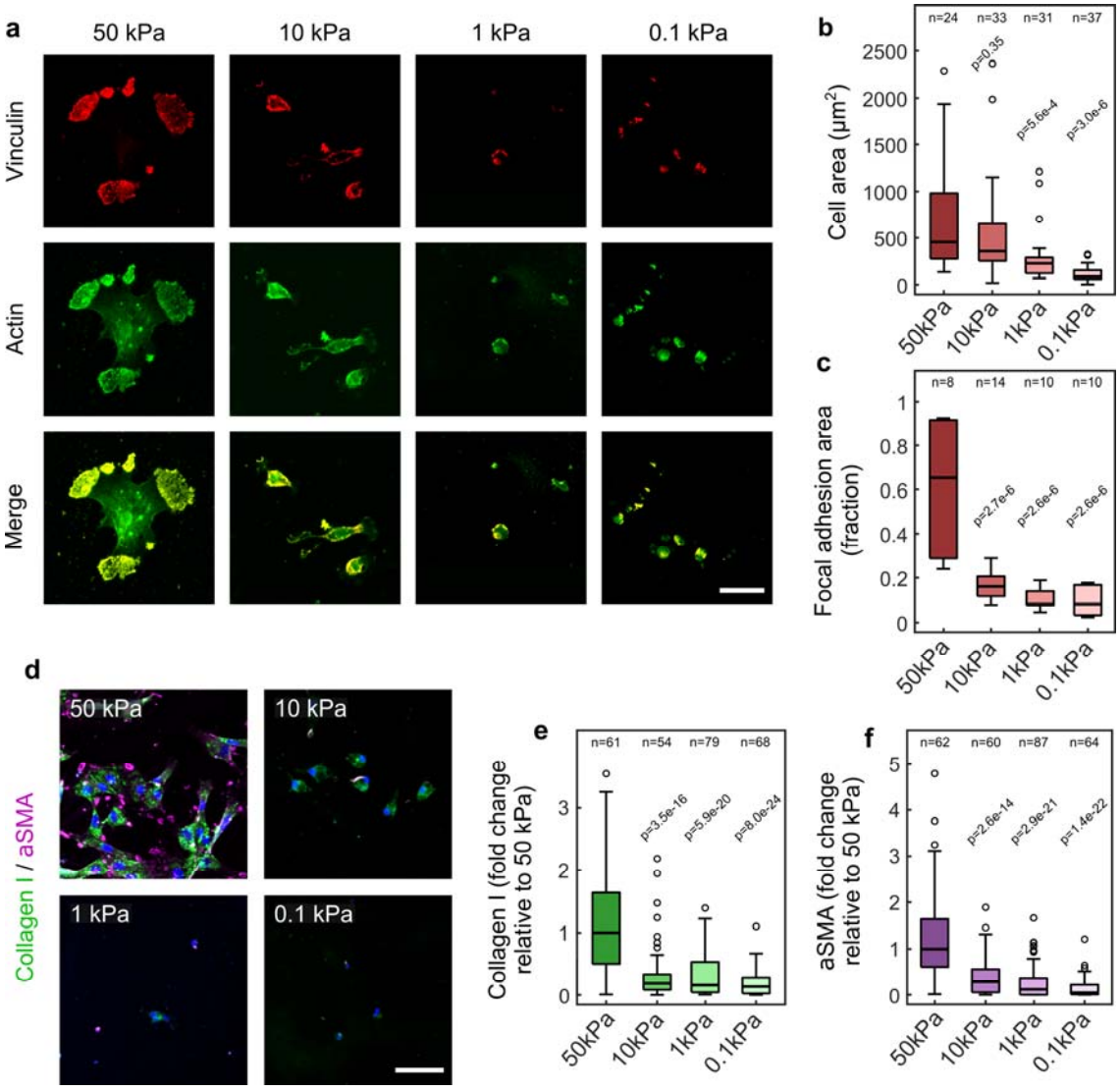

733

734 **Fig 1 | Substrates with a stiffness above that of the native tissue trigger fibrosis *in***

735 ***vitro*. a**, Maximum intensity projections of *z*-stack confocal images of nerve fibroblasts at 6

736 DIV cultured on polyacrylamide substrates of various stiffness (50, 10, 1 and 0.1 kPa shear

737 modulus), stained for cytoskeleton (actin) and focal adhesion (vinculin) markers. Cell

738 morphologies significantly changed on non-physiologically stiff (shear modulus of 50 kPa)

739 substrates. Scale bar: 30 μm. **b**,**c**, Box plots of fibroblast cell area (**b**) and focal adhesion

740 area (**c**). *n* = number of cells. **d**, Images of fibroblasts stained for myofibroblast markers

741 αSMA (magenta) and collagen I (green) show an increase in fibrotic phenotype on 50 kPa

742 gels. Cell nuclei stained with DAPI (blue) Scale bar: 60 μm. **e**,**f**, Box plots of relative stain

743 intensities for collagen I (**e**) and αSMA (**f**). *n* = number of cells. All statistical comparisons

744 done via one-way ANOVA followed by Dunnett's multiple comparisons test comparing to the

745 50 kPa condition. All experiments performed 3 - 4 times.

746

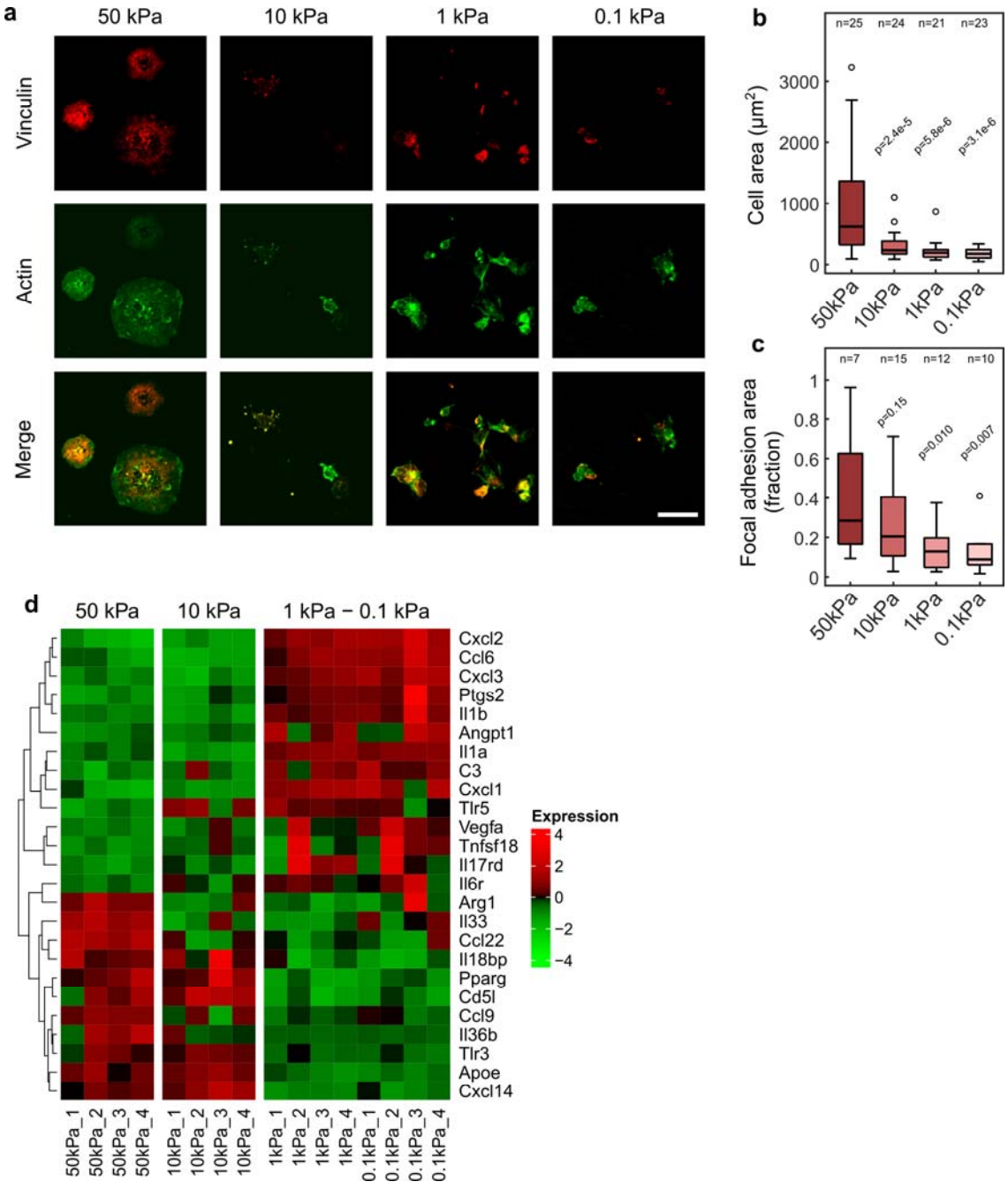

747

748 **Fig 2 | Substrates with a stiffness above that of the native tissue trigger macrophage**
749 **activation and changes in inflammatory profile *in vitro*. a**, Maximum intensity projections
750 of *z*-stack confocal images of bone marrow-derived macrophages at 6 DIV cultured on
751 polyacrylamide substrates of various stiffness (50, 10, 1 and 0.1 kPa shear modulus),
752 stained for cytoskeleton (actin) and focal adhesion (vinculin) markers. Cell morphologies
753 significantly changed on non-physiologically stiff (50 kPa) substrates. Scale bar: 30 µm. **b**,**c**,

754 Boxplots of macrophage cell area (**b**) and focal adhesion area (**c**). *n* = number of cells. All
755 statistical comparisons done via one-way ANOVA followed by Dunnett's multiple
756 comparisons test comparing to the 50 kPa condition. **d**, Heatmap of changes in inflammatory
757 differentially expressed gene (DEG) expression profile of macrophages at 3 DIV detected in
758 RNAseq (expression values represented as mean centred rlog-transformed counts).
759 Changes in markers such as *arg1, pparg, il1b,* and *ptgs2* indicate a switch to an M2-like
760 phenotype of macrophages grown on high stiffness substrates. Four samples analysed for
761 each substrate stiffness condition**.**

762

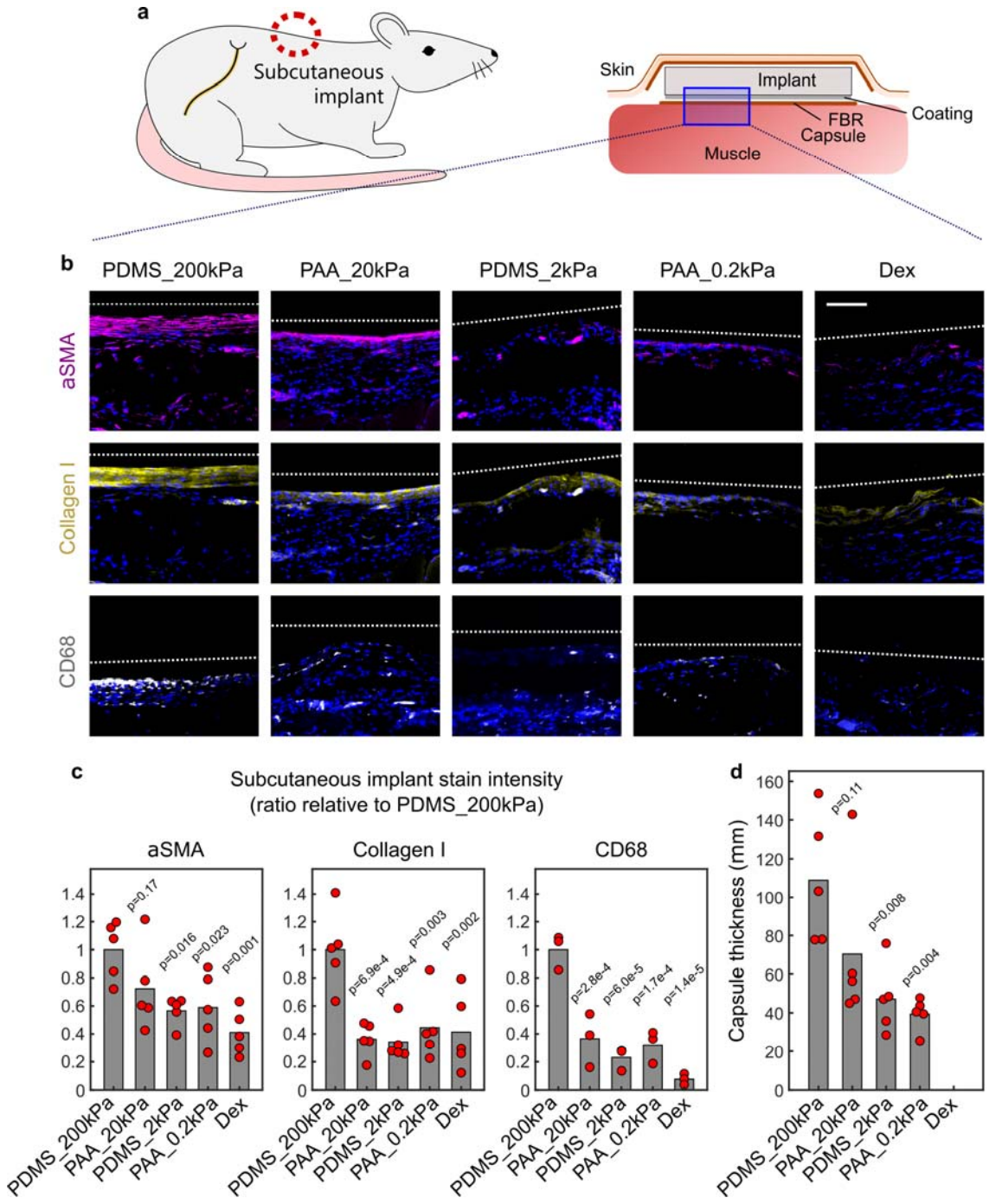

Fig 3 | Soft coatings significantly reduce foreign body reaction to subcutaneous implants 3 months post-implantation *in vivo*. **a**, Diagram of implant location and structure. Blue square represents area shown in images in **b**. **b**, *Z*-stack confocal images of subcutaneous tissue in response to implants of 200 kPa shear modulus silicone PDMS (PDMS_200kPa), or to implants coated with 20 kPa polyacrylamide hydrogel (PAA_20kPa),

2 kPa PDMS (PDMS_2kPa), 0.2 kPa polyacrylamide (PAA_0.2kPa), or PDMS impregnated with 10 mg/ml of the anti-inflammatory drug dexamethasone (Dex). Tissue is fluorescently labelled for myofibroblasts (αSMA), extracellular matrix components (collagen I), and macrophages (CD68). Approximate edges of implant are indicated by dashed white lines. All images show DAPI stains of nuclei (blue). FBR was significantly alleviated when the implant was coated with a soft material of $G \leq 2$ kPa. Scale bar: 100 μm. **c**, Plot of stain intensities. **d**, Plot of fibrotic capsule thickness. Quantification of thickness in Dex group absent as dexamethasone impeded formation of a structured boundary between tissue and implant. For all plots: bars represent mean, dots represent individual animals. $N = 5$ rats. Statistical comparisons carried out via one-way ANOVA followed by Dunnett's multiple comparisons test comparing groups to the PDMS_200kPa control condition.

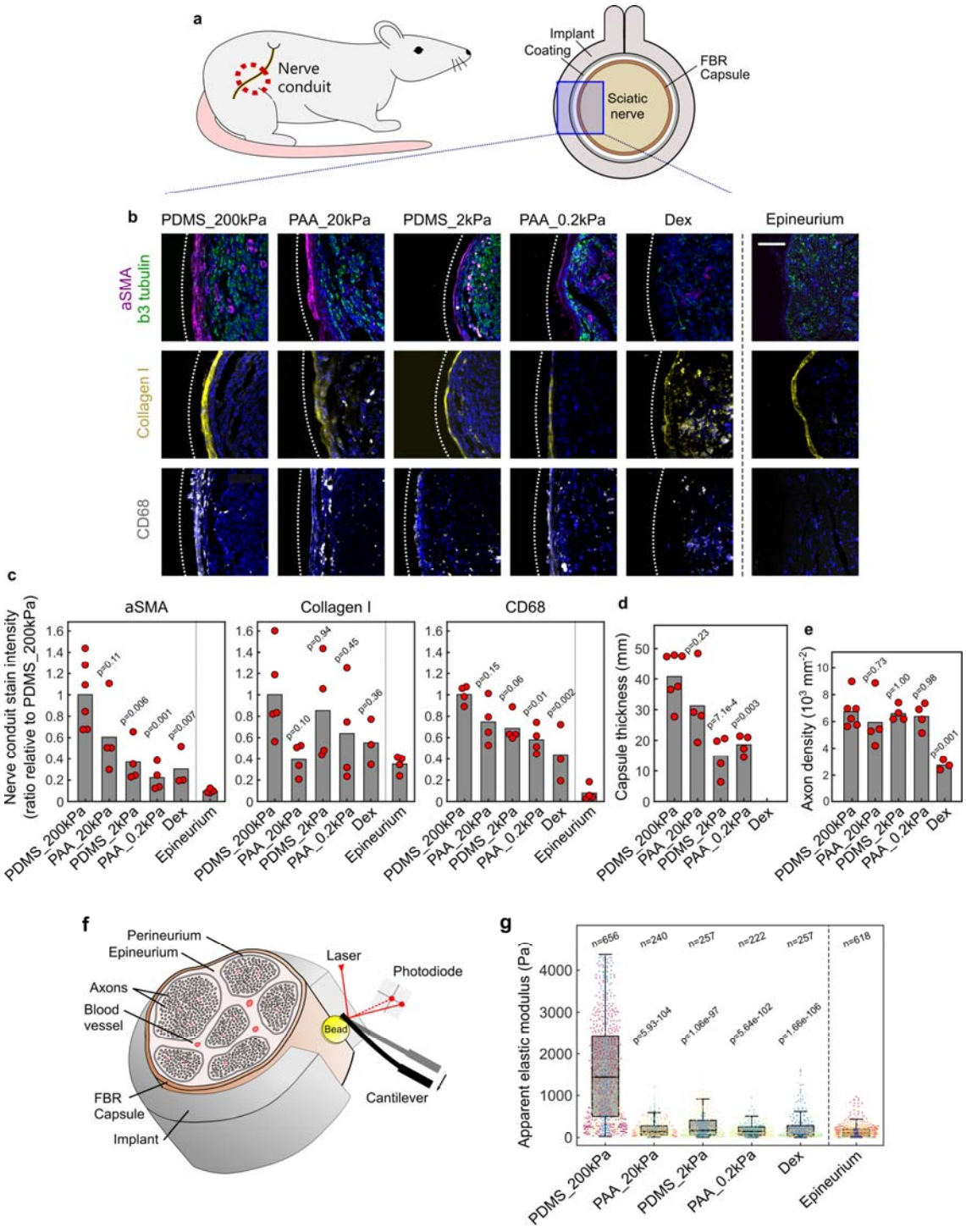

781

782 **Fig 4 | Soft coatings significantly reduce foreign body reaction to nerve conduits 3**

783 **months post-implantation *in vivo*. a**, Schematic of implant location and structure. Implants

784 had an internal diameter of 1.5 mm. Blue square represents area shown in images in **b**. **b**, *Z*-

785 stack confocal images of sciatic nerve tissue regenerated through conduits of 200 kPa shear

786 modulus silicone PDMS (PDMS_200kPa), or conduits coated with 20 kPa polyacrylamide
787 hydrogel (PAA_20kPa), 2 kPa PDMS (PDMS_2kPa), 0.2kPa polyacrylamide (PAA_0.2kPa),
788 or PDMS impregnated with 10 mg/ml dexamethasone (Dex). Approximate edges of implant
789 are indicated by dashed white lines. Tissue is fluorescently labelled for axons (β3 tubulin),
790 myofibroblasts (αSMA), extracellular matrix components (collagen I), and macrophages
791 (CD68). All images are stained for nuclei (DAPI, blue). Images of non-operated naïve nerves
792 are also included for comparison (epineurium). Softer coatings reduced cell activation and
793 fibrotic capsule thickness while permitting nerve regeneration. Dex-treatment, however, not
794 only abolished the fibrotic capsule but also nerve regeneration. Scale bar: 100 μm. **c**, Plot of
795 relative stain intensities. **d**, Plot of axon density in nerves 5 mm downstream of implantation
796 site. **e**, Plot of fibrotic capsule thickness. Quantification of thickness in Dex group absent as
797 dexamethasone impeded formation of a structured boundary between tissue and implant.
798 For all plots: bars represent mean, dots represent individual animals. *N* = 3 to 6 rats. **f**,
799 Diagram of *ex vivo* AFM setup for nerve tissue stiffness measurements. **g**, Box and scatter
800 plot of tissue stiffness values for tissue in proximity to the implants with various coatings,
801 showing a significant stiffening of tissue around implants with a stiff surface. Tissue stiffness
802 was similar around PDMS_2kPa, PAA_0.2kPa, and Dex-treated implants ($p > 0.05$). *n* =
803 number of measurements. Measurements taken on *N* = 3 to 6 rat nerves; measurements
804 taken from the same animal are depicted with the same colour. All statistical comparisons
805 carried out via one-way ANOVA followed by Dunnett's multiple comparisons test comparing
806 groups to the PDMS_200kPa control condition. Epineurium condition not included in
807 statistical analysis. Bonferroni-corrected Student's t-test used for comparisons to Dex group.

808

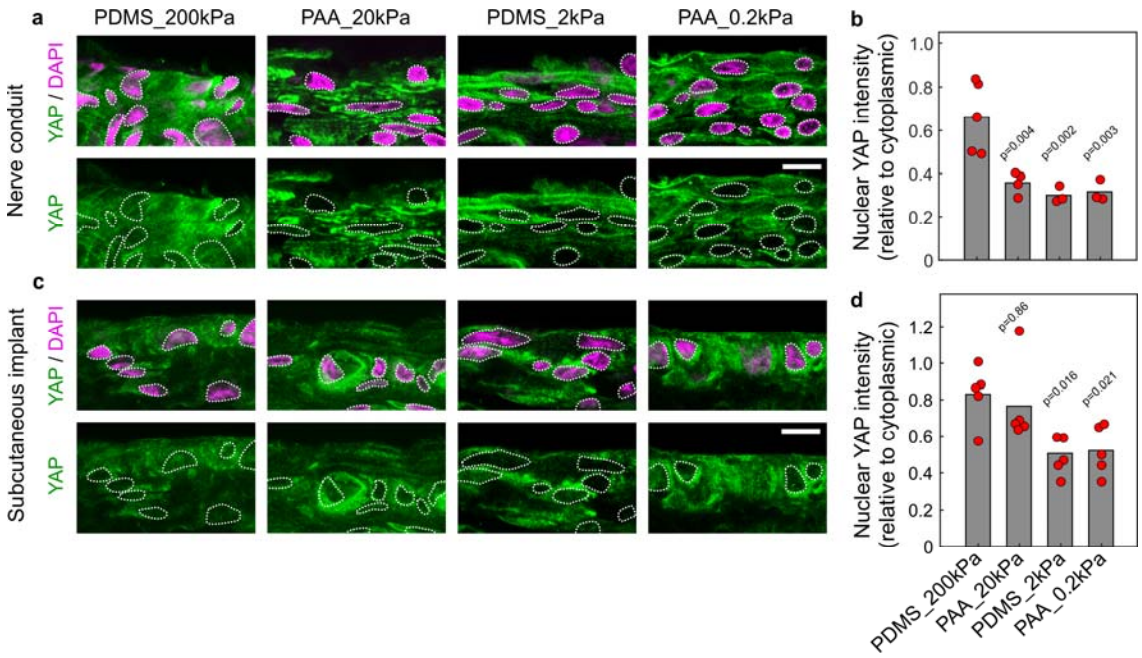

Fig 5 | Reduction in foreign body reaction *in vivo* correlates with exclusion of the mechanosensitive transcriptional regulator YAP from nuclei in tissues surrounding soft-coated implants. **a,c**, Confocal images of nerve (**a**) and subcutaneous tissue (**c**) stained for the transcriptional regulator YAP and nuclei (DAPI). Tissue was exposed to implants of 200 kPa shear modulus silicone PDMS (PDMS_200kPa), or to implants coated with 20 kPa polyacrylamide hydrogel (PAA_20kPa), 2 kPa PDMS (PDMS_2kPa), or 0.2 kPa polyacrylamide (PAA_0.2kPa), for 3 months. YAP preferentially localised into nuclei of cells in contact with stiff but not with soft-coated implants, indicating a mechanosensitive process. Nuclei delineated by dashed white lines. Scale bars: 10 μm. **b**,**d**, Plots of relative nuclear YAP intensities. Bars represent mean, dots represent individual animals. *N* = 3 to 5 rats (**b**) and *N* = 5 rats (**d**). All statistical comparisons carried out via one-way ANOVA followed by Dunnett's multiple comparisons test comparing groups to the PDMS_200kPa condition.